dissociation (restricted to slip plane) of an $a/2\langle 111\rangle$ dislocation into two parallel $a/4\langle 111\rangle$ partial screw dislocations.

Image simulations (*9*) were done to test whether the modification of the lattice image between the dissociated dislocation segments in Fig. 2A resulted from the occupancy of previously unfilled X and Z sites (*2*). A "doubling" in the image is seen at higher magnification where the faulted and unfaulted structures meet (Fig. 2D). The simulation for a thickness of 104.7 nm at a defocus of -50 nm most closely resembles the experimental images in the unperturbed crystal regions and at the dislocation. The model of filling X and Z voids at the dislocation is consistent with the apparent doubling of the lattice image.

Deviation from garnet stoichiometry (that is, the presence of impurities) in the stacking fault region may be expected to enhance or stabilize the dissociation of the $a/2\langle 111\rangle$ dislocation (*1*). However, no apparent inclusion or other preexisting defect is observed. Three possible explanations for this absence may be that (i) interstitial atoms that may stabilize dissociation are present in low concentrations and are not visible, (ii) atoms with nominally different valence may reside on an existing site (such as Fe(III) on X), which would not otherwise affect the structural image, or (iii) the dislocation has experienced motion after its formation as a growth defect and that the dissociation is glide-induced. The first two possibilities are intriguing because they imply that low quantities of dopant or solute atoms or slight deviations from stoichiometry may lead to dissociation in garnet and potentially in other complex silicates and oxides.

Evidence to support the stabilization of dissociated cores by trace amounts of solute is provided in Fig. 3, in which a grown-in dislocation has dissociated into a dipole of two $a/4\langle 111\rangle$ partial dislocations. However, this dissociation occurred by a nonconservative ("climbing") process, because the closure error of the dipole indicates that dissociation entailed loss of material equivalent to one unit cell (arrow). It is unlikely that these garnets were plastically deformed, so the only mechanism for the formation of this dissociated dipole would be the flux of vacancies to the precursor core segment, which would cause the small but observable dissociation through a Suzuki-type mechanism (*10*).

There are several important problems in mineral physics that are well suited for HRTEM analysis of dislocation cores. For example, the mechanism of the olivine-spinel transformation at 400-km depth in the mantle may depend on the dissociation of olivine defects (*11*). Plastic flow of the lower mantle may be strongly influenced by perovskite defect structures, and inferences have been made that the core regions of dislocations in perovskite are also dissociated (*12*). The crystal structures and electron scattering of olivine and perovskite are similar to garnet; recent reports of the imaging of dissociated olivine defects (*13*) demonstrate that HRTEM analysis of defects in dense oxides may be generally feasible.

REFERENCES AND NOTES

1. B. K. Smith, in *Metamorphic Reactions*, vol. 4 of *Advances in Physical Geochemistry*, A. B. Thompson and D. C. Rubie, Eds. (Springer-Verlag, New York, 1985), pp. 98–117.
2. Burgers vectors are described by their length in terms of the lattice parameter a and the crystallographic orientation in Miller index notation. For garnet, which is cubic, the [111] direction is symmetrically equivalent to eight directions (one per octant of the unit cell); this is indicated by the convention $\langle 111\rangle$ that signifies the group of symmetrically related [111] directions. The group of symmetrically related (hkl) planes is conventionally written as $\{hkl\}$.
3. J. Rabier, P. Veyssiere, T. Grilhe, *Phys. Status Sol. A* **35**, 259 (1976).
4. J. Rabier, P. Veyssiere, H. Garem, *Philos. Mag. A* **44**, 1363 (1981).
5. J. W. Matthews and T. S. Plaskett, *Phys. Status Sol. A* **35**, 577 (1976). R. K. Mishra and G. Thomas, *J. Appl. Phys.* **49**, 1876 (1978).
6. D. R. Veblen, in *Point Defects in Minerals*, vol. 31 of *Geophysical Monographs*, R. N. Schock, Ed. (American Geophysical Union, Washington, DC, 1984), pp. 122–131; ——— and P. R. Buseck, *Am. Mineral.* **65**, 599 (1980).
7. Garnets were single crystals of grossular [$(Ca_{2.9}Fe^{II}_{0.1})(Al_{1.9}Fe^{III}_{0.1})Si_{3.0}O_{12}$] obtained from Belvedere Mountain near Eden Mills, Vermont. Fieldwork in this area demonstrates that no appreciable plastic deformation has affected these garnets [A. H. Chichester, A. Albee, W. M. Cady, *U.S. Geol. Surv. Prof. Pap.* **1016** (1978)] and our TEM observations did not detect evidence consistent with appreciable plastic deformation (for example, slip plane traces or recovered dislocation frameworks). The HRTEM images of the dislocations were obtained from thick regions (100 to 150 nm) of atom-milled foils of these crystals. The micrographs were taken with a JEOL-4000EX microscope, a 400-keV instrument with a point-to-point resolution of ~0.17 nm. This microscope is equipped with a high-brightness LaB_6 electron gun that enables direct image viewing at electron-optical magnifications of 1×10^6 times without loss of resolution from excessive incident-beam divergence. The objective lens has a spherical aberration coefficient (C_S) of 1.0 ± 0.1 mm, as determined by optical diffractogram analysis.
8. F. M. Allen and P. R. Buseck, *Am. Mineral.*, in press; G. R. Rossman, *Geol. Soc. Am. Abstr. Program* **18**, 525 (1986).
9. Simulations were calculated with the Arizona State University versions of multislice-image simulation programs [K. Ishizuka, *Ultramicroscopy* **5**, 55 (1980); ——— and N. Uyeda, *Acta Cryst. A* **33**, 740 (1977)]. Images were calculated in the $[0\bar{1}1]$ direction for a projected unit cell that was 1.185 nm by 1.675 nm ([100] and [011], respectively). The cell was divided along (011); one-half of the cell consisted of normal grossular garnet structure, with calcium in X, aluminum in Y, and silicon in Z (160 atoms), whereas the other half contained these atoms plus calcium and silicon atoms that were displaced by $a/4\langle 111\rangle$ (208 atoms), that represent the stuffed holes at the stacking fault interface. The entire cell was divided along $[0\bar{1}1]$ into eight slices, each 0.209 nm thick, and a phase grating was calculated for each slice. Five hundred slices were integrated to yield a total thickness of 104.7 nm; a propagation function was applied between the slices. Diffracted waves (4096) were used in the potential distribution and phase-grating calculations with a $(\sin\theta)/\lambda$ limit of 30 nm^{-1}. Spherical aberration, voltage, beam divergence, and defocus spread were fixed at 1.0 mm, 400 kV, 0.8 mrad, and 10 nm, respectively, corresponding to the JEOL-4000EX instrument. A maximum resolution of 0.17 nm was assumed; the effects of beam tilt and crystal tilt were not considered. Calculations were stored for thicknesses of 5.23 nm (every 25 slices) up to 104.7 nm and for defocus values between ~10 nm to ~100 nm in increments of ~5 nm.
10. P. Veyssiere, J. Rabier, H. Garem, J. Grilhe, *Philos. Mag. A* **38**, 61 (1978).
11. H. W. Green II, *Geophys. Res. Lett.* **11**, 817 (1984).
12. J. P. Poirier, J. Peyronneau, J. Y. Gesland, G. Brebec, *Phys. Earth Planet. Inter.* **32**, 273 (1983).
13. M. Kitamura *et al.*, *Nature (London)* **328**, 143 (1987).

14. Work supported by NSF grants EAR-8408168 (P.R.B.), EAR-8517548 (B.K.S.), and DMR-8306501 (ASU Facility for HREM).

6 July 1987; accepted 17 September 1987

Horizontal Plate Motion: A Key Allocyclic Factor in the Evolution of the Great Barrier Reef

P. J. Davies, P. A. Symonds, D. A. Feary, C. J. Pigram

The Great Barrier Reef complex of northeastern Australia thins dramatically and becomes younger from north to south. These variations are a consequence of the Cenozoic northward movement of the Indian-Australian plate. The temperate climatic conditions that applied off northeast Australia during the early Tertiary were progressively replaced by tropical conditions. The present-day south-to-north facies distribution along the eastern Australian continental margin mimics the Cenozoic vertical facies sequence through the northern part of the Great Barrier Reef region.

The Great Barrier Reef of northeastern Australia, which is comprised of approximately 2500 individual reefs and extends for ~2000 km from 9° to 24°S, is the largest reef province on the earth (Fig. 1). Studies in the past 10 years (*1–3*) have defined the major autocyclic factors that affect reef growth. From these results a model has been constructed in

Bureau of Mineral Resources, General Post Office Box 378, Canberra 2601, Australia.

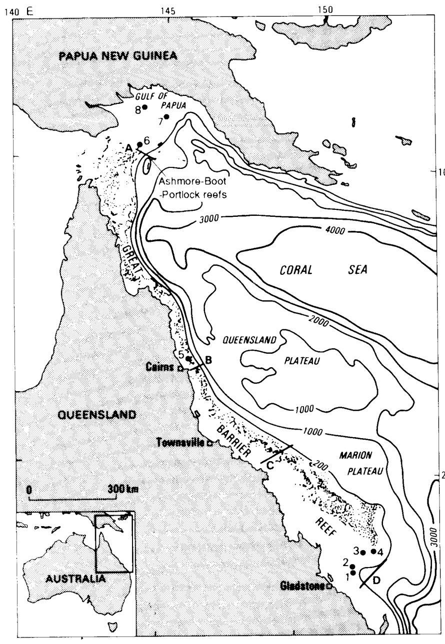

Fig. 1. Location of the major physiographic elements off northeast Australia, showing sites of drill holes (circles) and schematic sections (lines A to D). Drill holes are numbered as follows: 1, Heron Island; 2, Wreck Island; 3, Capricorn; 4, Aquarius; 5, Michaelmas Cay; 6, Anchor Cay; 7, Pasca; and 8, Borabi.

which episodes of high energy reef growth during transgressive events alternate with exposure surfaces that represent low sea level stands (*3*).

Past attempts to understand the history of reef growth off northeast Australia (*4–6*) have been based principally on seismic data from oil exploration in the Gulf of Papua and on sparse drill hole data at the northern and southern ends of the Great Barrier Reef. One of these studies (*4*) concluded that reef growth commenced in the Miocene throughout the region, and this conclusion went unchallenged in many subsequent reports. An analysis of recent Bureau of Mineral Resources seismic data from the central part of the Great Barrier Reef has cast doubt on this inference; it indicated that significant reef growth in this particular area probably did not begin until the Pleistocene (*7*). The important question is whether reef growth was initiated contemporaneously throughout the region, or whether regional controls exerted influences that resulted in sequential initiation of reef growth.

Data collected by the Bureau of Mineral Resources during the 1985 cruises of the R.V. *Rig Seismic* (*8*) confirmed that buried reefs exist beneath the outer part of the northern Great Barrier Reef, and that a much thicker reef section occurs in this area than in the central and southern parts of the reef province. These conclusions, together with further analysis of earlier data, have provided new insights into the factors affecting growth of the Great Barrier Reef and, in particular, account for the latitudinal age and thickness variation. These conclusions also define constraints on reef initiation and show that latitudinal plate motion is one of the major allocyclic factors controlling reef growth.

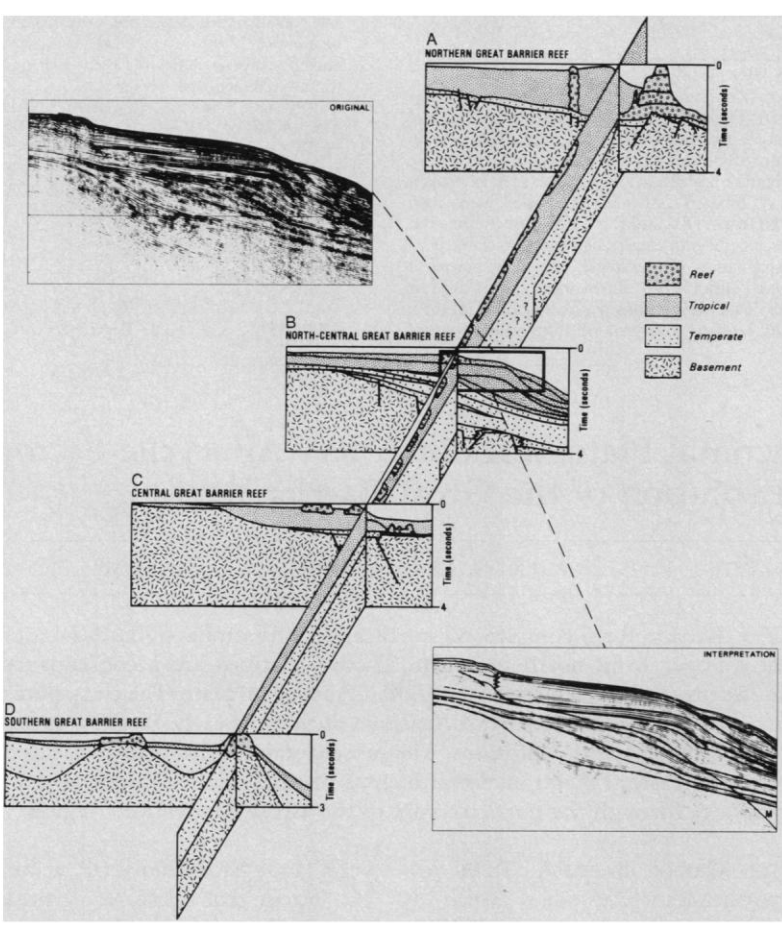

Fig. 2. Schematic north-to-south section illustrating the thickness variations of tropical and temperate facies. The northward-thickening tropical wedge implies that reef growth began earlier in the north than in the south. A representative seismic section illustrating the nature of seismic sequences forming the outer shelf–upper slope from the north-central Great Barrier Reef is also shown (M, multiplied).

The thickness of the reefs and the age of initial reef growth vary over the length of the reef province (Fig. 2). Data from drill holes (*9–11*) and more recent seismic data (*8*) in the northern Great Barrier Reef and the Gulf of Papua permit a more precise interpretation of the chronology of reef growth in this area. Drill hole data show that late early to middle Miocene reefs occur in the Borabi 1 and Pasca C1 holes (Fig. 3), and that reefs from at least the Pliocene occur in the Anchor Cay 1 well (*10*). Seismic data indicate that these reefs represent part of an extensive Miocene barrier (*12, 13*) and platform reef (*11*) complex that extended at least 100 km north of the modern Great Barrier Reef. Seismic sections over the Ashmore-Boot-Portlock reef trend and adjacent shelf reveal a 1.5-km reef section surrounded and overlain by fluviodeltaic sediments. A tie to a well in the Gulf of Papua indicates that reef growth in this section began during the early to middle Miocene.

In the central Great Barrier Reef, 8000 km of intermediate-resolution seismic data (*7*) have helped define a reef section 150 to 300 m in thickness that is surrounded and underlain by a nonreef section up to 3 km thick (Fig. 2). These reefs formed during high sea level growth phases. A Plio-Pleistocene age for initiation of reef growth in this area is based on a tentative seismic tie to Deep Sea Drilling Project Site 209 on the Queensland Plateau and analysis of sea level–related sequences (*7*). A drill hole on Michaelmas Cay (Fig. 3) in the central Great Barrier Reef also supports this age conclusion (*14*).

The most reliable constraints on the age and thickness of reefs in the southern Great Barrier Reef region are provided by the Heron Island and Wreck Reef drill holes (Fig. 3) and the Aquarius 1 and Capricorn 1A exploration wells (*15, 16*). Data from these holes indicate that the oldest parts of the 100- to 150-m-thick reef section are of Pleistocene age. Seismic lines in this region show no evidence of any extensive buried reef development below the Pleistocene section. The above data indicate that the Great

Fig. 3. Stratigraphy and lithology of drill holes in the Great Barrier Reef (**A**) and Gulf of Papua (**B**) (TD, total depth).

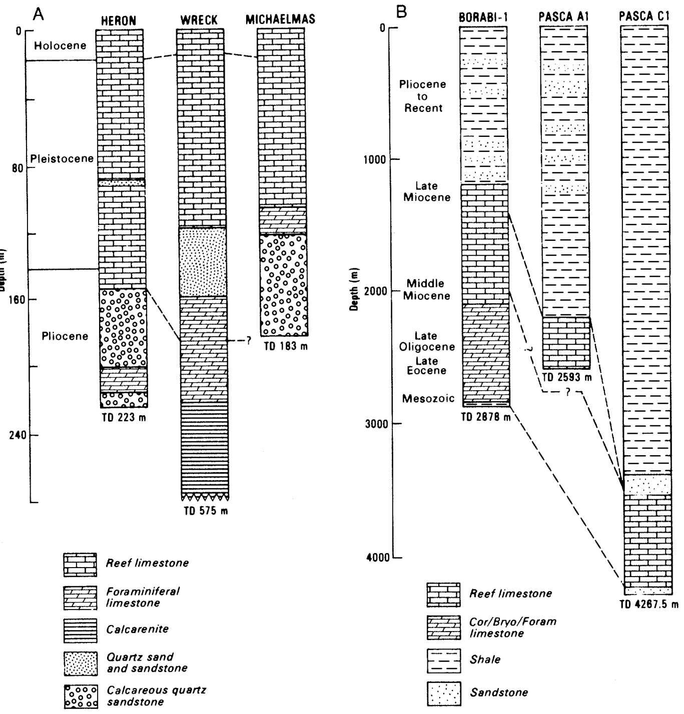

Barrier Reef thins and becomes younger from north to south.

During the past decade, plate tectonic (*17*) and magnetostratigraphic (*18*) studies have provided a detailed reconstruction of the movement of the Indian-Australian plate throughout the Tertiary (Fig. 4). The latitudinal error limits on the plate motion curve for the Miocene to Recent period are of the order of only 4°. These studies show that at the end of the Oligocene, the Great Barrier Reef region was between 21° and 36°S. During the following 24 million years, the region moved almost directly northward to its present location between 9° and 24°S.

Latitudinal plate movement would have resulted in marked climatic changes along the eastern Australian shelf. Such changes should be clearly recorded in the continental margin sediments of the Great Barrier Reef region, with sediments deposited under temperate climatic conditions overlain by a southward-thinning wedge of sediment with tropical affinities. Analysis of northward plate movement, together with consideration of paleoceanographic and paleoclimatic variables (*19*), indicates that (i) the transition from temperate to tropical climatic conditions in the northern part of the Great Barrier Reef occurred between 16 million and 25 million years ago; (ii) the central Great Barrier Reef experienced a temperate climate until 10 million to 15 million years ago; and (iii) the southern region became tropical only in the last few million years.

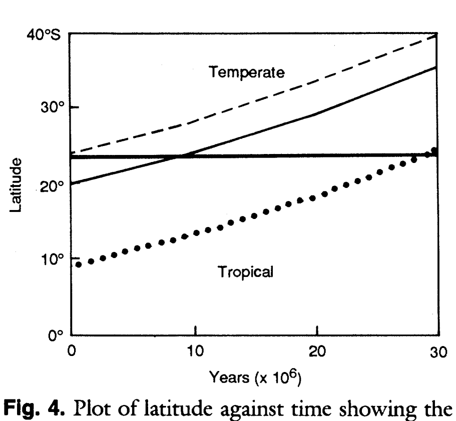

Fig. 4. Plot of latitude against time showing the position of the northern (dotted line), central (solid line), and southern (dashed line) Great Barrier Reef during the Tertiary. The temperate-tropical boundary is based on latitude 23.5°S (the Tropic of Capricorn).

Coral reefs in the modern Great Barrier Reef develop under tropical conditions, where annual mean surface seawater temperatures are generally greater than 20°C (*20*). The transition between the thick early to middle Miocene reef section in the north and the thin Pleistocene reef section in the south of the Great Barrier Reef region may therefore be explained as a direct consequence of the progressive temperate to tropical climatic transition arising from the northward movement of Australia.

A test of our hypothesis is provided by a comparison of present-day variations in latitudinal sediment facies with the vertical facies succession encountered in drill holes; that is, does Walther's law of correlation of facies apply? The present-day facies distribution on the outer continental shelf of eastern Australia is a function of latitude (*20*), with three clearly defined facies that reflect latitudinal temperature and salinity variability. These facies are (i) tropical carbonate and clastic sediments, dominated by coral and *Halimeda* debris, north of 24°S; (ii) subtropical rhodolith-encrusting foram-bryozoan facies between 24° and 28°S; and (iii) temperate branching foram-bryozoan mollusk facies south of 28°S.

This same facies sequence occurs vertically in the Borabi 1 exploration well (Fig. 3) in the northern Great Barrier Reef area, thereby confirming the hypothesis that horizontal surface and vertical subsurface facies variations in the Great Barrier Reef province are a sensitive indicator of the Cenozoic plate motion of Australia.

REFERENCES AND NOTES

1. J. F. Marshall and P. J. Davies, *Coral Reefs* **1**, 21 (1982).
2. P. J. Davies and D. Hopley, *Bur. Miner. Resour. J. Aust. Geol. Geophys.* **8**, 237 (1983).
3. P. J. Davies, in *Perspectives on Coral Reefs*, D. J. Barnes, Ed. (Brian Clouston, Canberra, 1983), pp. 69–106.
4. J. J. Tanner, *UN Econ. Comm. Asia Far East Miner. Resour. Dev. Ser.* **41**, 283 (1969).
5. A. R. Lloyd, in *Biology and Geology of Coral Reefs*, O. A. Jones and R. Endean, Eds. (Academic Press, New York, 1973), vol. 1, pp. 347–366.
6. P. A. Symonds, in *Proceedings: Inaugural Great Barrier Reef Conference*, J. T. Baker, R. M. Carter, P. W. Sammarco, K. P. Stark, Eds. (James Cook Univ. Press, Townsville, Australia, 1983), pp. 151–157.
7. ——, P. J. Davies, A. Parisi, *Bur. Miner. Resour. J. Aust. Geol. Geophys.* **8**, 277 (1983).
8. P. J. Davies *et al.*, *Aust. Bur. Miner. Resour. Rep. 255*, in press.
9. G. P. McDonagh and B. W. Knuth, *Phillips* et al. *Borabi No. 1. Well Completion Report* (Phillips Australian Oil Company, Brisbane, 1968).
10. T. W. Oppel, *Tenneco-Signal Anchor Cay Number 1 Offshore Queensland, Well Completion Report* (Tenneco Oil Company, Houston, 1969).
11. W. A. Patterson, *Phillips* et al. *Pasca No. 1 Well Completion Report* (Phillips Australian Oil Company, Brisbane, 1969).
12. R. A. Wise, in *Petroleum*, vol. 3 of *Economic Geology of Australia and Papua New Guinea*, R. B. Leslie, H. J. Evans, C. L. Knight, Eds. (Australasian Institute of Mining and Mineralogy, Melbourne, 1976), pp. 494–499.
13. N. C. Tallis, *Aust. Pet. Explor. Assoc. J.* **15**, 15 (1975).
14. H. C. Richards and D. Hill, *Great Barrier Reef Bores, 1926 and 1937—Descriptions, Analyses, and Interpretations* (Reports of the Great Barrier Reef Committee, University of Queensland, Brisbane, 1942).
15. C. T. Carlsen and T. C. Wilson, *Gulf-A.O.G. Capricorn No. 1A Well Completion Report* (Australian Gulf Oil Company, Brisbane, 1968).
16. ——, *Gulf-A.O.G. Aquarius No. 1 Well Completion Report* (Australian Gulf Oil Company, Brisbane, 1968).
17. R. A. Duncan, *Tectonophysics* **74**, 29 (1981).
18. M. Idnurm, *Geophys. J. R. Astron. Soc.* **83**, 419 (1985).
19. A compilation of paleoceanographic and paleoclimatic data for northeast Australia shows that during the middle Eocene–early Oligocene, surface water temperatures decreased despite the northward plate movement. The Neogene increase in latitudinal thermal gradient and northward movement combined to produce steadily increasing surface water temperature in the region, as it became more distant and oceanographically isolated from the development of Antarctic glaciation and higher latitude

cooling events. The minor low-latitude surface water temperature falls were essentially offset by northward movement of the region.
20. J. F. Marshall and P. J. Davies, *Bur. Miner. Resour. J. Aust. Geol. Geophys.* 3, 85 (1978).
21. We thank our colleagues in the Bureau of Mineral Resources who contributed to discussions on this paper.

22 June 1987; accepted 27 October 1987

Quantitative Three-Dimensional Optical Tomographic Imaging of Supersonic Flows

GREGORY W. FARIS* AND ROBERT L. BYER

Three-dimensional imaging of the density of nitrogen in a supersonic expansion from a nozzle by means of beam-deflection optical tomography is described. With a very simple apparatus, images could be obtained with high absolute accuracy, high spatial resolution, and wide dynamic range.

OPTICAL DIAGNOSTIC TECHNIQUES are useful for making measurements in many transparent systems, including fluid flows, flames, plasmas, and the atmosphere. Optical techniques are nonintrusive and allow fast measurements. However, accurate spatially resolved measurements of real physical parameters are difficult to obtain with optical techniques. Measurement techniques that involve multiple-photon processes and scattering, such as coherent anti-Stokes Raman spectroscopy (CARS) (*1*), fluorescence imaging (*2*), Rayleigh scattering (*3*), and Mie scattering (*4*), can give spatially resolved measurements but do not easily yield quantitative images. Measurements of optical phase (by means of interferometry, holography, or beam-deflection techniques, for example) or absorption are more direct. These correspond to the measurement of the real or imaginary part of the index of refraction, respectively. However, these techniques give values that are integrated along the line of sight. With tomographic techniques (*5*), multiple views of integrated measurements through a flow field may be used to reconstruct spatially resolved values of a physical quantity in the system. Thus optical tomography allows measurement of spatially resolved parameters with the accuracy of integrated techniques.

Optical tomography has other advantages. Optical access is only required in the plane being imaged. This is important for systems such as jet engines and tokamaks, where imaging perpendicular to the region of interest is impossible. In addition, because each plane may be imaged independently, many planes may be measured at the same time, allowing simultaneous acquisition of three-dimensional images.

Optical tomography has been demonstrated with both phase (*6–12*) and absorption (*13–15*) measurements. Phase measurements can give spatially resolved values of density in single-component fluid flows (*6*). In constant pressure systems, phase measurements can give information about temperature (*7, 10*) or composition (*7*). Absorption tomography can be used to measure both temperature and concentration variations, which is useful in combustion studies (*15*).

Tomography based on phase measurements has the advantage that the measurements may be made on any transparent flow, and no tunable laser is required. Tomography has been performed with phase measurements from beam deflection (*6–8*), interferometry (*9, 10*), and holography (*11, 12*). Because interferometric and holographic techniques involve fringe counting, there is ambiguity in the sign of phase change across a fringe and a limitation on the dynamic range. Beam-deflection techniques do not have phase-sign ambiguities and continue to be useful when large gradients would create too many fringes to resolve or when vibration could wash out fringes. Beam-deflection techniques can be very sensitive as well. We have demonstrated sensitivity down to 35 nanoradians, which is equivalent to a change equal to 1/23,000 of an interference fringe over the laser-beam spot size (0.81 mm). As no reference beam is necessary for beam-deflection measurements, stability is required only on a single optical path.

Another significant advantage of beam-deflection measurements is that they can be applied to larger systems. If a system under investigation is proportionally scaled to a larger size, the beam deflections remain the same size. That is, although the path length scales up, the gradients scale down, and the net deflection remains the same. This is in contrast to fringe-counting techniques for which the number of fringes increases proportionally to the integration length and may reach an impractical number.

As a demonstration of the capabilities of beam-deflection optical tomography, we have performed measurements of density in a supersonic expansion of nitrogen gas from a nozzle. The variation of the equation of state in such an expansion is well understood (*13*) and provides a good check for our measurements. The flow is also very reproducible. We have examined supersonic expansions from single and multiple nozzles. For the single expansion measurements, a tapered nozzle with a half angle of 5.5° and a throat diameter of 0.84 mm was used.

We have measured beam deflections in a simple manner, using a helium-neon laser beam, an 80-mm focal length transform lens, and a position-sensitive (split-element) detector, as shown in Fig. 1. The laser beam is deflected on transversing the supersonic expansion because of the gradients in the index of refraction. The transform lens is positioned one focal length from the position-sensitive detector. For an ideal lens and small deflections, all rays incident on the lens at a given angle are linearly mapped to a unique position in the focal plane of the lens. Thus the position-sensitive detector can directly measure the beam-deflection angle. A second 60-mm focal length lens is used to focus the laser beam, and this improves the spatial resolution in the expansion. A projection, or single view, through the supersonic expansion is taken by scan-

Edward L. Ginzton Laboratory of Physics, Stanford University, Stanford, CA 94305.

*Present address: Department of Physics/Atomic Physics, Lund Institute of Technology, Post Office Box 118, S-221 00 Lund, Sweden.

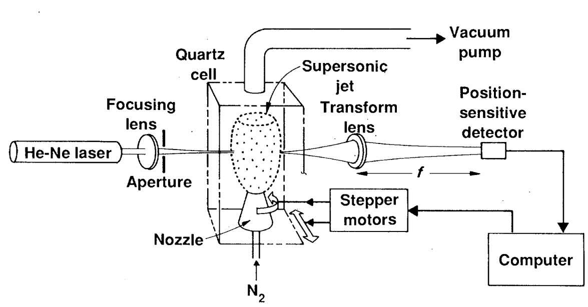

Fig. 1. Diagram of gas-flow, optical-imaging, and data-acquisition systems for beam-deflection optical tomography. The focal length of the transform lens (f) is 80 mm.